Pergamon

Int. J. Solids Structures Vol. 35, Nos. 5–6, pp. 365–381, 1998

0020–7683/98 $19.00 + .00

PII: S0020–7683(97)00035–87

DETERMINATION OF MONOTONIC STRESS–STRAIN CURVE OF HARD MATERIALS FROM ULTRA-LOW-LOAD INDENTATION TESTS

S. JAYARAMAN,† G. T. HAHN,† W. C. OLIVER,‡ C. A. RUBIN† and P. C. BASTIAS†

† Center for Materials Tribology, Vanderbilt University, Nashville, TN-37235, U.S.A. ‡ Metals and Ceramic Division, Oak Ridge National Laboratory, Oak Ridge, TN-37831, U.S.A.

(*Received* 18 *April* 1996; *in revised form* 13 *January* 1997)

Abstract—A method has been proposed to determine the stress-strain curve of hard materials from ultra-low-load indentation tests using geometrically similar indenters. The hardness-flow stress, and characteristic plastic strain-cone angle correlations, for conical indenters, were obtained from a number of calculations with different stress–strain curves using the finite element code ABAQUS. The flow stress values thus obtained, lie between that predicted by the slip line field theory and the spherical cavity expansion model. These correlations do not assume any deformation mode, and are thus valid for a wide range of hardness to elastic modulus ratio. The validity of the proposed method was checked by determining the monotonic stress-strain curve of 1070 steel from ultra-low-load indentation tests performed in the present study. Also, the stress–strain curves of copper and steel were obtained from macroscopic hardness values reported by Atkins and Tabor (Atkins, A.G. and Tabor, D. (1965) Plastic indentation in metals with cones. *Journal of the Mechanics and Physics of Solids* **13**, 149–164.). The predicted stress-strain curves agree well with the known properties of these materials. These correlations were then used to determine the monotonic stress–strain curve of silicon nitride. © 1997 Elsevier Science Ltd.

INTRODUCTION

Theoretical analyses

Indentation tests have long been used to evaluate the strength of metals and coatings. The approach is based on direct relations between the applied indenter load per unit contact area (hardness) and the (plastic) flow strength of the material. In the past, hardness tests exploited relatively large indentations which simplified the task of measuring the load and indentation area. Determining the plastic properties of hard, brittle materials like silicon nitride, from indentation tests requires ultra-low-load indentations to prevent cracking. Such ultra-low-load indentations, however, make it very difficult to obtain a direct measurement of the contact area.

Doerner and Nix (1986) have suggested a method to determine the contact area at peak load from the unloading part of the load-displacement curve. Their method relies on the assumption that the contact area is a constant during the initial unloading stages. Oliver and Pharr (1992) analyzed the unloading-reloading indentation load-depth curves of a number of materials ranging from aluminum to sapphire using a Berkovich indenter. They found that the contact area changes continuously right from the onset of unloading. Pethica *et al.* (1983) have developed instrumentation for accurately recording the load-depth data of indentations as small as 20 nanometers.

Prandtls' (1920) slip line field solution for a flat punch on a semi-infinite medium is one of the pioneering works attempting to relate the mean contact pressure (or hardness, H) to the resistance to local plastic deformation. Bishop *et al.* (1945) have discussed the indentation of ductile materials by cylindrical punches with conical heads. They obtained a theoretical expression relating the hardness H and yield strength σ, by analyzing the plastically deformed zone as the expansion of a spherical cavity in an elastic plastic solid with an internal hydrostatic pressure. Tabor (1951) obtained a simple linear relation ($H = C\sigma$) between the flow stress and hardness based on the solution using the slip line field theory for rigid-perfectly plastic materials.

In the case of materials that produce comparable elastic and plastic deformations, the slip line field theory underestimates the corresponding flow stress. Marsh (1964) points out that the slip line field theory when applied to glasses, predicts flow stresses well below the brittle fracture stresses. Samuels and Mulhearn (1957) and Mulhearn (1959) show, by plotting equal strain contours that material is often displaced radially outwards from the indentations rather than towards the surface as envisaged in the slip line field theory. Thus, by assuming a mode of deformation suggested by Bishop *et al.* (1945) and Hill, (1950), Marsh (1964) and Hirst and Howse (1969) found excellent correlation between the hardness and flow stress. However, the constants differed from the theoretical solution; this was attributed to differences in radial constraint between a spherical cavity expanding in an infinite body and that of a hemi-spherical cavity in a semi-infinite body. By ensuring compatibility between the volume of material displaced by the indenter and that accommodated by elastic expansion, Johnson (1970) included the effect of indenter geometry. Rubinstein (1981) has given an excellent review of these semiempirical approaches to indentation tests.

Numerical analyses

The theoretical solutions obtained by the use of simple models described above depend largely on the development of plastic zones under the indenter. The experimentally observed plastic zones, even for macroscopic indentations, do not agree with the assumption made by the slip line field theory. Also, for a given indenter geometry, the spherical cavity expansion model fails for high elastic modulus to flow stress ratio. Thus, it becomes essential to resort to numerical techniques to obtain the mechanical properties (hardness, elastic modulus, etc.) from sub-micron load-displacement curves.

Lee *et al.* (1972) have performed finite element analyses of ball indentation. They conclude that the computed load-displacement curve, plastic zone development and indentation pressures are in good agreement with those obtained experimentally for heat-treated steel SAE4340. Bourcier *et al.* (1985), have performed numerical and experimental studies of sub-micron indentations. Tanega and Hurkx (1986) have presented an iterative procedure to estimate the plastic part of stress-strain curves of ductile metal coating from Brinell indentation tests. However, their method cannot be applied for hard materials.

Bhattacharya and Nix (1988) have demonstrated the applicability of finite element techniques to simulate the load-displacement of sub-micrometer indentations. They also conclude from the analysis of such small indentations that the plastic zone shapes do not correspond to those assumed by either the rigid die model or the spherical cavity expansion model (1991). Cai an Zhou (1992) have demonstrated, using finite element analyses, that at very low loads elastic recovery does not account for the apparent variation in hardness. Very recently, Giannakopoulos *et al.* (1994), have performed a three dimensional finite element analysis of Vickers indentation.

The objective of the present study is to obtain the plastic part of the stress-strain curve of silicon nitride from ultra-low-load indentations using geometrically similar indenters. A procedure is presented to obtain (i) hardness-flow stress correlation that is independent of the mode of deformation, and, (ii) the representative plastic strain in the complex plastic strain field below such indenters. The validity of the proposed method is tested by determining the known monotonic stress-strain curve of 1070 steel.

EXPERIMENTAL PROCEDURE

The indentation tests were performed using the NANOINDENTER® II setup at Oak Ridge National Laboratory, Oak Ridge, TN. A detailed description of the setup can be found elsewhere (Oliver and Pharr, 1992; Oliver, Nanoindenter® reference manual, 1992).

The tests on 1070 steel and silicon nitride samples were performed using a Berkovich and a cube corner indenter. The three sided pyramidal Berkovich indenter and the cube corner have a nominal angle of 65.3° and 35.3° between the face and the vertical axis, respectively. The indentations using the Berkovich indenter were performed at a constant loading rate of 2000 μN/sec, and monotonic loading was continued to a peak load of 100

mN. The loading rate was reduced to 100μN/sec, and loading was continued to a peak load of 10 mN when the tests were performed using a cube corner indenter. This reduction in loading rate and peak load were done in order to avoid crack formation. Pharr *et al.* (1993) have demonstrated the reduction in load required to initiate cracks when a Berkovich indenter is replaced by a cube corner.

A load controlled unloading followed the initial monotonic loading. The unloading was done at 100% of the initial loading rate and continued until 95% of the peak load was removed. This unloading part of the load-depth was used to obtain the hardness of the samples following the method suggested by Oliver and Pharr (1992). All tests were done at room temperature.

ANALYTICAL PROCEDURE

Finite element model

An axisymmetric finite element model of a Berkovich indenter and a cube corner indenting a semi-infinite half-space was developed using the multi-purpose finite element code ABAQUS (Fig. 1). A reduction in the computational time and the inherent complexity involved in three dimensional modeling were achieved by using conical indenters to model the three sided pyramidal indenters. The half-angle of the cone was chosen such that the projected area of the cone, for any depth of penetration, equaled that of the pyramidal

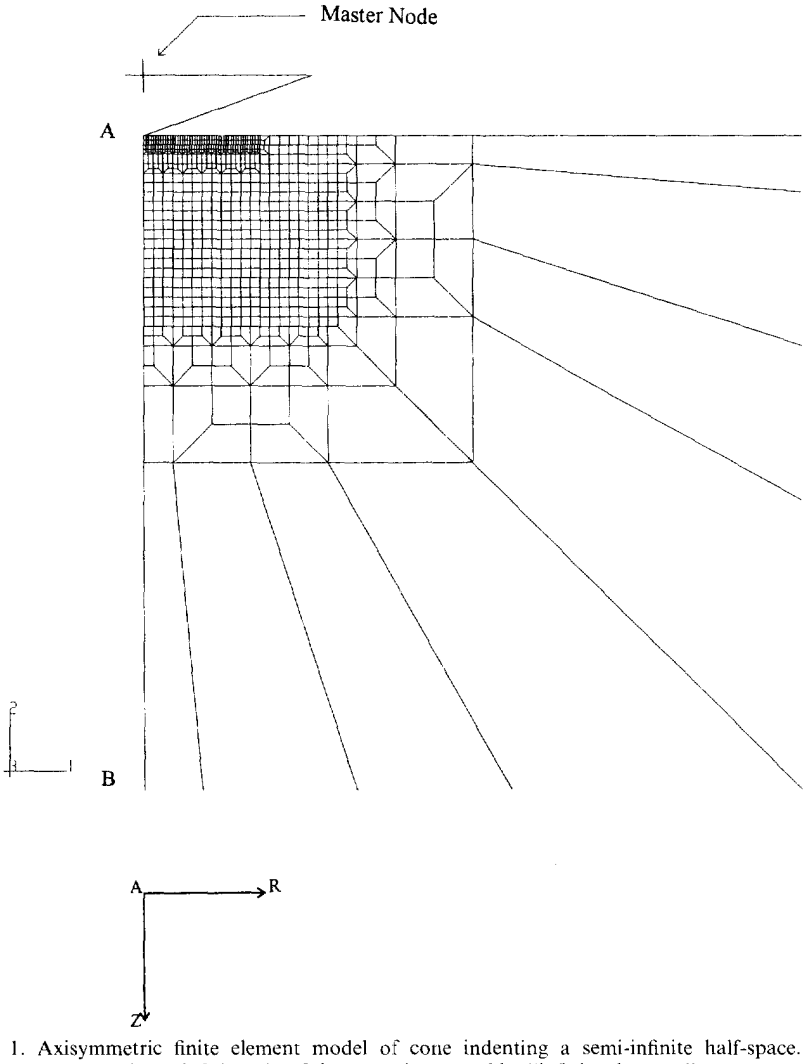

Fig. 1. Axisymmetric finite element model of cone indenting a semi-infinite half-space. The unbounded domain of the target is covered by "infinite elements".

indenters. This half-angle equals 70.3° and 42.3° for the Berkovich indenter and the cube corner, respectively. Since any typical indentation experiment would involve blunting of the indenter tip, the cone tip was smoothed by a sphere of radius much smaller than the indentation depth; this also eliminates any possible convergence errors due to sharp corners.

Four noded linear axisymmetric elements were used to model the half-space. Contact between the rigid cone and the specimen was modeled using rigid surface contact elements. Friction between the indenter and the material surface was taken as zero. By symmetry, the nodes along the axis AB of the cylinder were constrained to move only along the longitudinal z-direction. Mapped infinite elements were used to model the unbounded domain of the target.

The movement of the rigid cone was achieved by prescribing downward displacement (negative z direction) to a single master or reference node in the rigid body (Fig. 1). Subsequent unloading was done by removing the prescribed indenter displacement at peak load. This results in a linear reduction of the peak reaction force to a prescribed minimum value of 5% of the maximum reaction force. The rigid body was constrained against any rotation.

An elastic modulus of 207 GPa and Poisson's ratio of 0.3 was taken for the 1070 steel. For the silicon nitride sample, the elastic modulus and Poisson's ratio taken were 315 GPa and 0.26, respectively. Isotropic hardening behavior was assumed during monotonic loading for both the samples.

RESULTS AND DISCUSSION

Figures 2 and 3 show the variation of the average equivalent plastic strain beneath the indenter with strain hardening index n, for conical indenters with half angles of 70.3° and 42.3°, respectively. The average equivalent plastic strain $\bar{\varepsilon}_p$ in the plastically deformed volume V_p is defined as:

$$\bar{\varepsilon}_p = \frac{1}{V_p}\sum_{1}^{M} \varepsilon_i \Delta V_i \tag{1}$$

where ε_i is the equivalent plastic strain at the centroid of element i, ΔV_i is the volume of

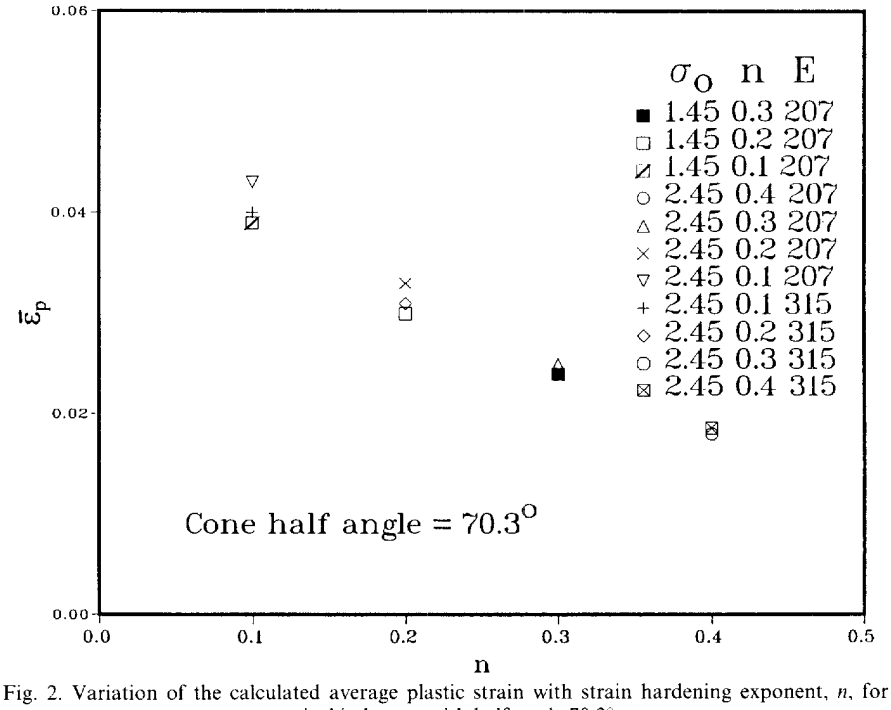

Fig. 2. Variation of the calculated average plastic strain with strain hardening exponent, n, for conical indenters with half-angle 70.3°.

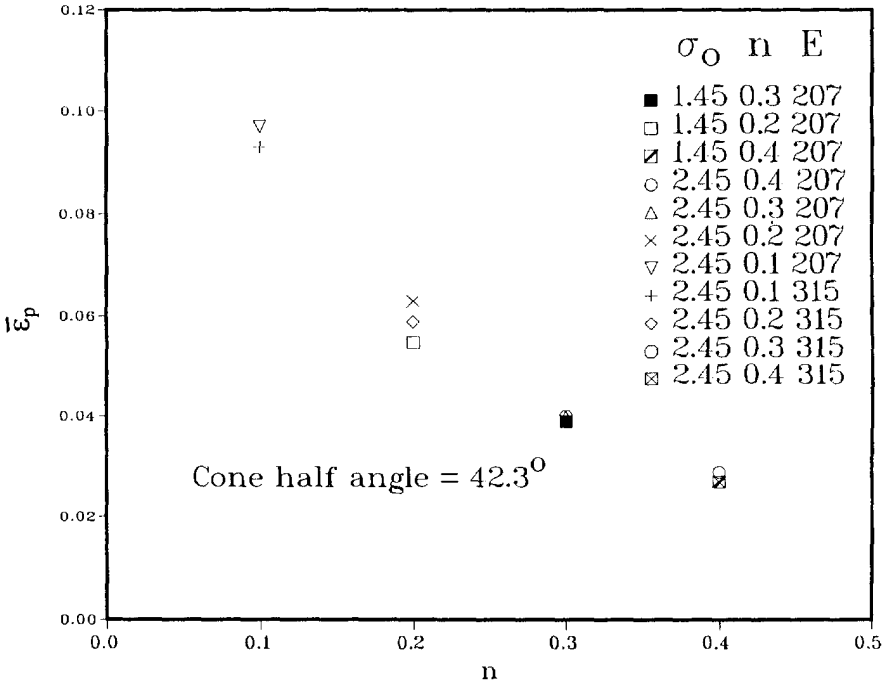

Fig. 3. Variation of the calculated average plastic strain with strain hardening exponent, n, for conical indenters with half-angle 42.3°.

element i, and M is the total number of elements whose centroidal equivalent plastic strain value is non-zero (above 0.002). Thus,

$$V_p = \sum_{1}^{M} \Delta V_i.$$

In the case of geometrically similar indenters, it is customary to define a single value of the plastic strain characteristic of the indenter geometry. This is referred to as the characteristic plastic strain. As shown in Figs 2 and 3, the dependence of $\bar{\varepsilon}_p$ on the strain hardening index n does not make it a suitable candidate for characteristic plastic strain. However, it is possible to choose a single value of plastic strain magnitude close to the average strain following the procedure described below.

The spherical cavity expansion model expresses the hardness to elastic modulus ratio (H/E) as a function of the flow stress to elastic modulus ratio (σ/E) for materials that are very hard or elastic. Also, the linear hardness-flow stress correlation obtained from the slip-line filed theory can be rewritten in terms of H/E and σ/E. Due to the $1/E$ dependence in these relations, the elastic modulus was used as the normalizing parameter. As a first step in developing the hardness-flow stress correlation using the elastic modulus as the normalizing parameter, the dependence of equivalent plastic strain ε_p on the equivalent flow stress σ was given by the simple Ramberg-Osgood equation:

$$\varepsilon_p = K\left(\frac{\sigma}{E}\right)^N. \tag{2}$$

Any definition of characteristic plastic strain should be such that it is (i) dependent on the geometry of the self-similar indenter, and (ii) independent of the depth of penetration. For a given material, an experimentally determinable parameter that can satisfy both these conditions is the hardness (H). If the characteristic plastic strain (ε_p) is related to the hardness (H) by a function similar to eqn 2, we have:

$$\varepsilon_p = K'\left(\frac{H}{E}\right)^{N'}. \tag{3}$$

Such a definition identifies the material being indented in terms of the new parameters K' and N', while satisfying conditions (i) and (ii), mentioned above. Thus, for a given indenter geometry, equating eqs 2 and 3 gives a hardness-flow stress relation of the form,

$$\frac{H}{E} = A\left(\frac{\sigma}{E}\right)^{B} \tag{4}$$

where

$$A = \left(\frac{K}{K'}\right)^{1/N'}, \quad \text{and} \quad B = \frac{N}{N'}$$

At this stage, the characteristic plastic strain (ε_p), is not yet defined. For a given material, i.e., given K and N, the material parameters K' and N' can be so chosen that they yield a constant value of A and B. The following paragraph describes the method used to obtain the constants A, B, and the characteristic plastic strain for a given indenter geometry.

A curve of the form given by eqn 2 was used to describe the plastic strain-stress correlation of the material in the finite element model. Twelve different combinations of initial yield strength σ_o, elastic modulus E, and strain hardening exponent N were used to obtain a set of points $[(\sigma/E)_j, (H/E)_j; j = 1,2,\ldots,12]$. The flow stress to elastic modulus ratios, $(\sigma/E)_j$, were obtained from eqn 2 for an arbitrary value of characteristic plastic strain, $\varepsilon_p = \varepsilon_p^j$. The $(H/E)_j$ values were directly obtained from the hardness, H, defined as the ratio of the applied load (P) to the projected indenter material contact area (A). The value of ε_p^j that yielded the best fit curve (maximum correlation coefficient, R_j, of the type given by eqn 4, to the set of points, $[(\sigma/E)_j, (H/E)_j; j = 1,2,\ldots,12]$, was taken as the characteristic plastic strain for the given indenter geometry. The hardness-flow stress correlation as expressed by eqn 4 does not assume any mode of deformation beneath the indenter.

The calculated characteristic plastic strain values following the procedure described in the preceding paragraph were 0.07 and 0.225 for a cone with a half-angle of 70.3° and 42.3°, respectively. Figure 4 compares the calculated representative strains with those obtained experimentally for macroscopic indents by Atkins and Tabor (1965) for a number of indenter geometries. The characteristic plastic strain and the corresponding flow stress obtained from the hardness values, from a given indenter geometry, thus provide a single point on the plastic part of the stress-strain curve.

Figures 5 and 6 show the calculated variation of hardness with flow stress for the 70.3° and 42.3° cones, respectively. Figure 5 also shows the experimentally observed variation (Marsh, 1964) obtained by fitting the data points from a number of materials to a curve of type given by the spherical cavity expansion model. The predicted curve, assuming rigid plastic deformation using the slip line field theory, is also shown. The values calculated in the present study lie between these two extremes. Figure 7 compares the calculated H/E vs σ/E curves for the two conical indenters. This was done to check if the proposed method reliably correlates the micro-hardness to the flow stress independent of the mode of deformation. As seen in this figure, for $H/E < 0.16$, there is very little difference between the two curves, although they characterize two very different modes of plastic deformation beneath the indenter. This is reasonable to expect, since,

$$A = \left(\frac{K}{K'}\right)^{1/N'}, \quad \text{and} \quad B = \frac{N}{N'},$$

and hence, are independent of the self-similar indenter geometry. A single curve that approximates the two nearly similar curves in Fig. 7 was found to have the form:

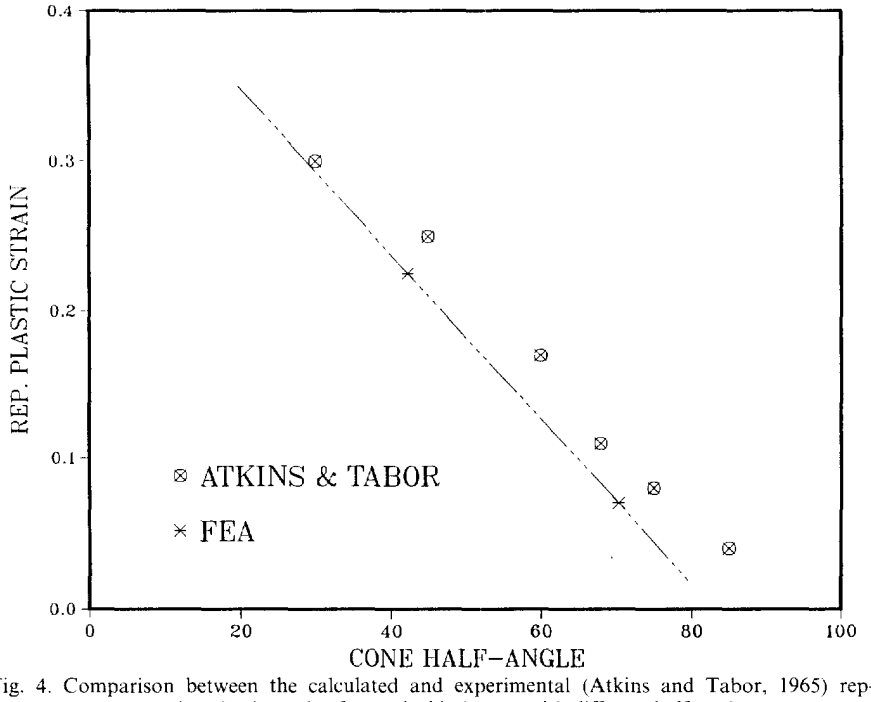

Fig. 4. Comparison between the calculated and experimental (Atkins and Tabor, 1965) representative plastic strains for conical indenters with different half-angles.

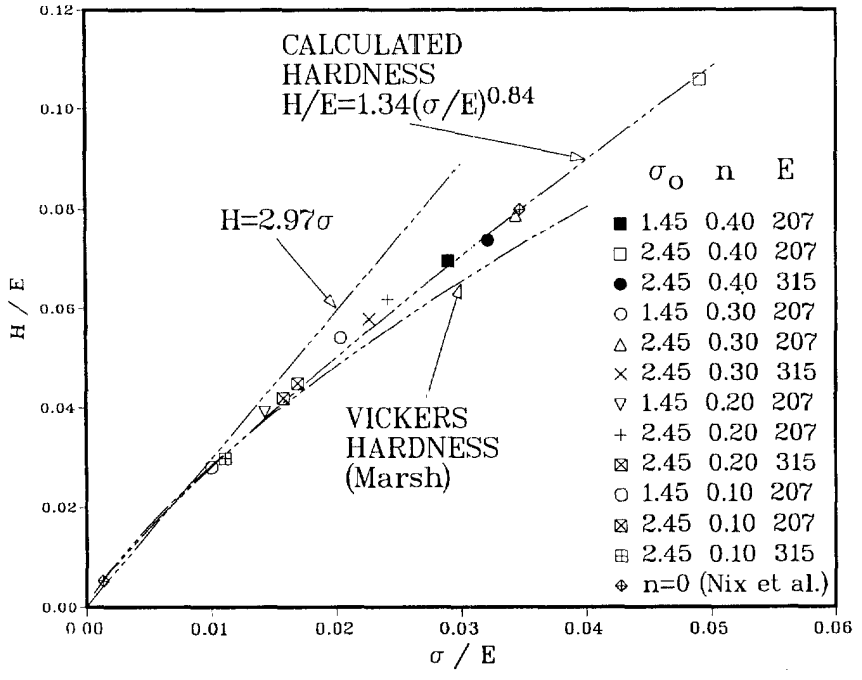

Fig. 5. Variation of the calculated hardness to elastic modulus ratio with the flow stress to elastic modulus ratio for a conical indenter with half-angle of 70.3°. Flow stress at a plastic strain of 0.07 was used.

$$\frac{H}{E} = 1.7\left(\frac{\sigma}{E}\right)^{0.92}. \tag{5}$$

The above equation was used to determine the flow stress from the hardness values. The characteristic plastic strain and the corresponding flow stress for two different indenter

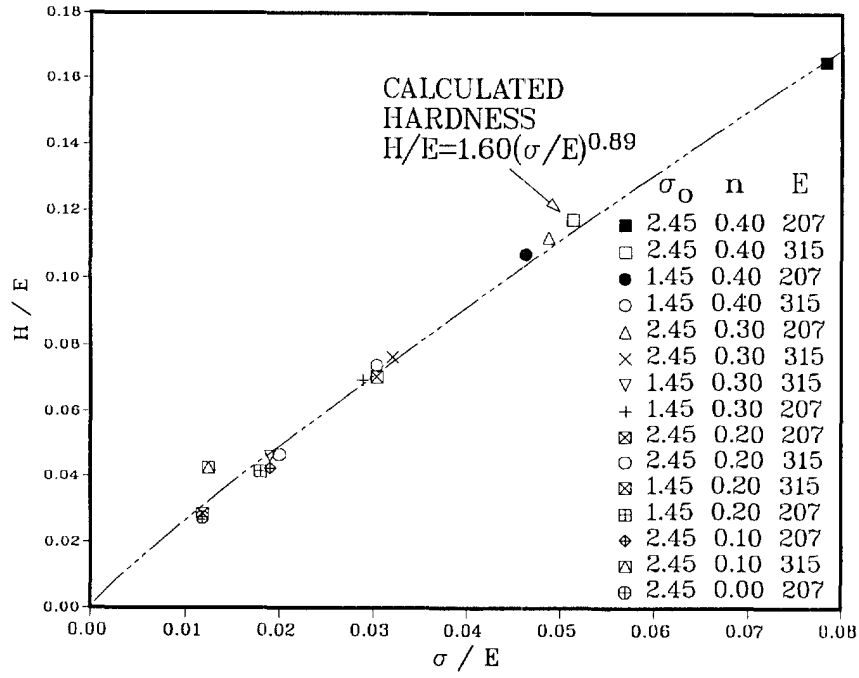

Fig. 6. Variation of the calculated hardness to elastic modulus ratio with the flow stress to elastic modulus ratio for a conical indenter with half-angle of 42.3°. Flow stress at a plastic strain of 0.225 was used.

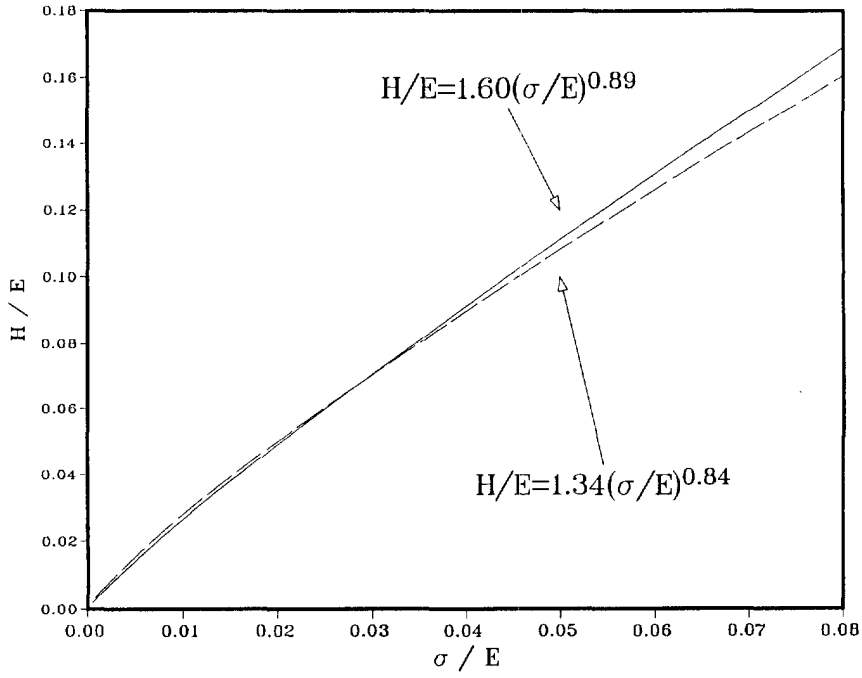

Fig. 7. Comparison of H/E vs σ/E curves for two conical indenters with half-angles of 70.3° and 42.3°.

geometries were then fit to a curve of type $\sigma = k\varepsilon_p^n$. It is worth mentioning that eq 5 is valid only for $H/E < 0.16$, the range of values used to evaluate the characteristic plastic strain.

Figures 8 and 9 show the calculated dependence of the contact depth to total indentation depth ratio (h_c/h) on the hardness to reduced modulus ratio (H/E_R), for conical indenters with half-angles of 70.3° and 42.3°, respectively. The general equation relating h_c/h and H/E_R was assumed to have the same form as that obtained by Oliver and Pharr

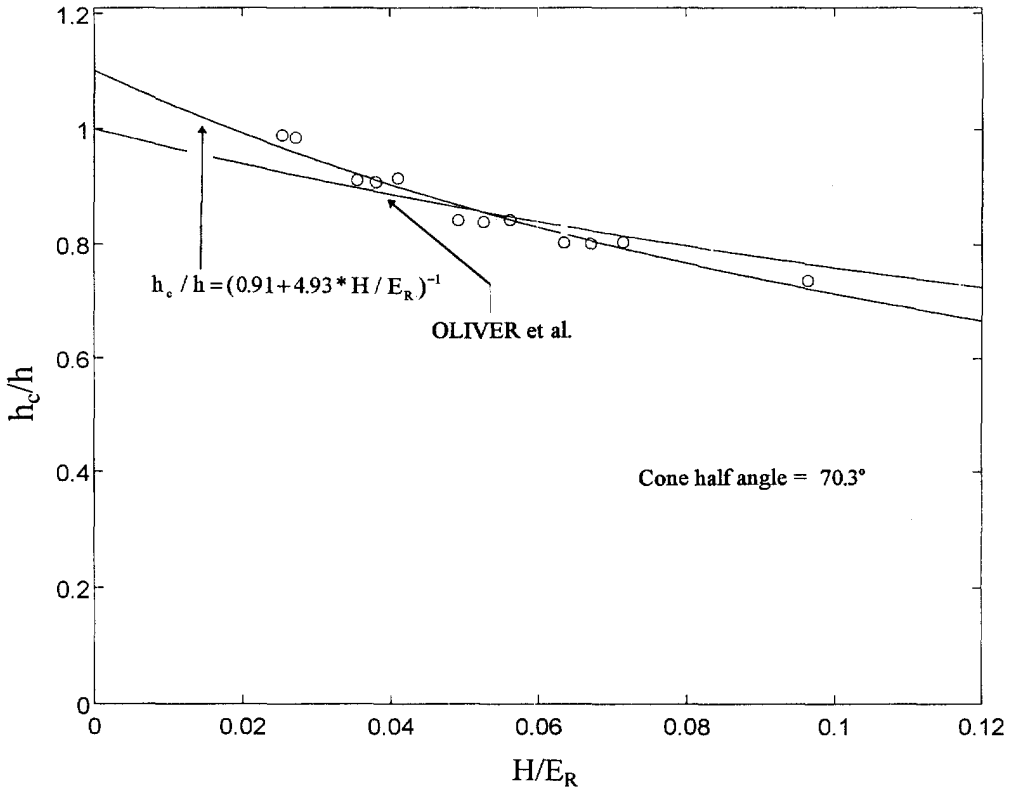

Fig. 8. The dependence of contact height on hardness for a conical indenter with half-angle of 70.3°. The contact height and hardness are normalized with respect to total penetration depth, h_c, and reduced elastic modulus, E_R, respectively.

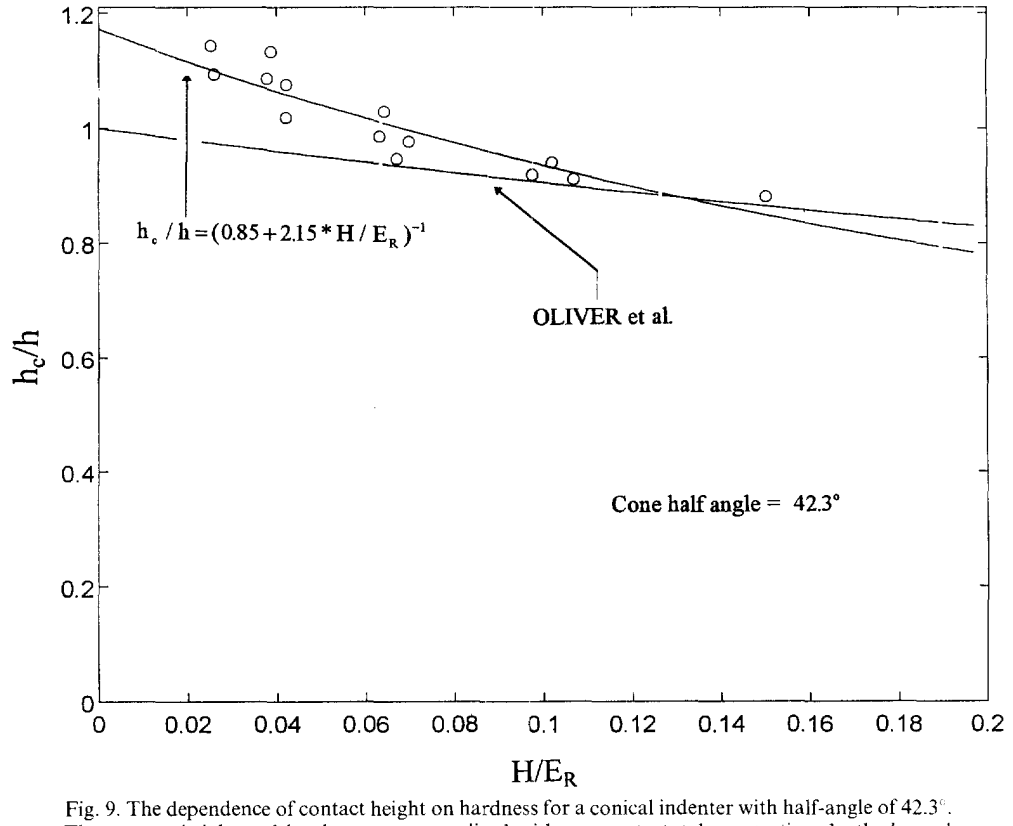

Fig. 9. The dependence of contact height on hardness for a conical indenter with half-angle of 42.3°. The contact height and hardness are normalized with respect to total penetration depth, h_c, and reduced elastic modulus, E_R, respectively.

(1992). The corresponding equation, and the constants fitting the calculated data for the two indenters are:

$$\left(\frac{h_c}{h}\right) = \frac{1}{(\xi + \Omega H/E_R)}$$

$$\xi = 0.91, \Omega = 4.93 \text{ for the } 70.3^\circ \text{ indenter;}$$

$$\xi = 0.85, \Omega = 2.15 \text{ for the } 42.3^\circ \text{ indenter.} \quad (6)$$

For a given contact depth, h_c, the reduced modulus E_R, can be expressed in terms of the slope of the unloading curve at peak load, S (Sneddon. 1965; Oliver and Pharr, 1992), and area of contact at peak load, A as:

$$S = \frac{2}{\sqrt{\pi}} E_R \sqrt{A}$$

$$A = \alpha h_c^2$$

$$\alpha = 24.56 \text{ for } 70.3^\circ \text{ indenter}$$

$$\alpha = 2.601 \text{ for } 42.3^\circ \text{ indenter} \quad (7)$$

The hardness of the material is given the relation:

$$H = \frac{P_{\max}}{A} \quad (8)$$

where A is the contact area obtained from eqn 7. The total depth of indentation, h, peak load, $P_{\max}$, and slope, S, were obtained from the experimental load-displacement curves. Equations 6, 7, and 8, were solved simultaneously to determine the contact depth, reduced modulus, and the hardness of the material being indented. Typical experimental load-displacement curves for 1070 steel and silicon nitride samples, using Berkovich and cube corner indenters, are shown in Figures 10–13.

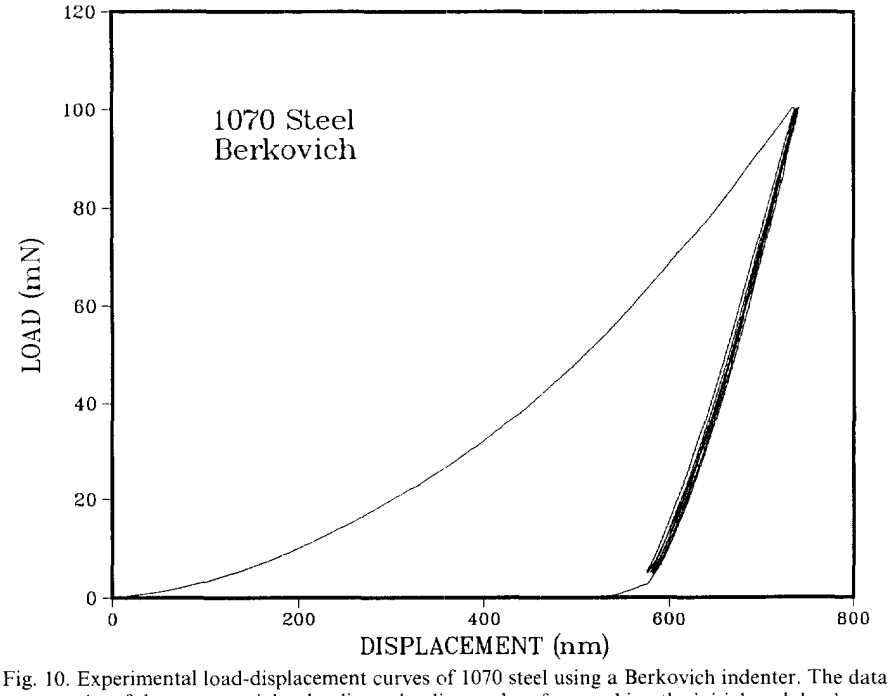

Fig. 10. Experimental load-displacement curves of 1070 steel using a Berkovich indenter. The data consist of three sequential unloading-reloading cycles after reaching the initial peak load.

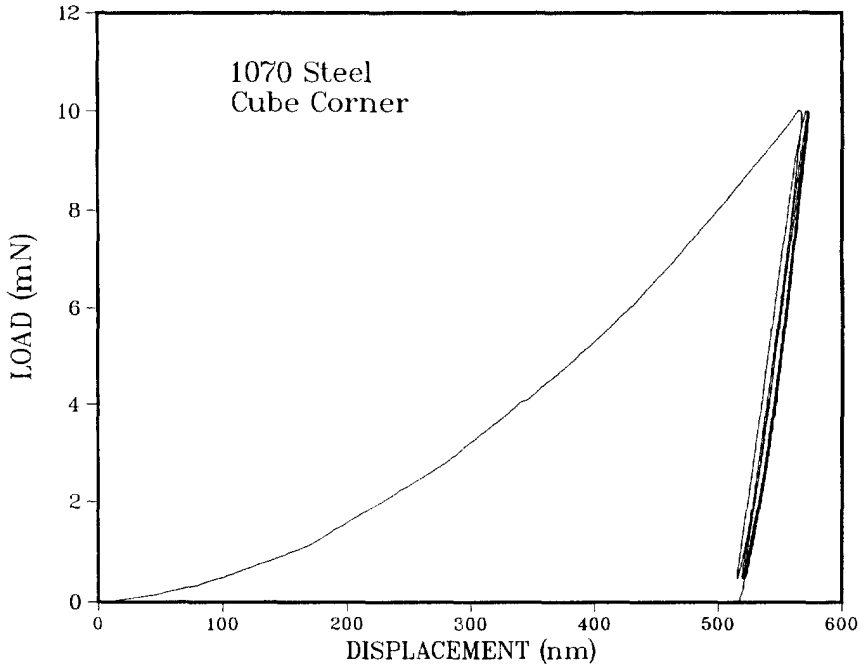

Fig. 11. Experimental load-displacement curves of silicon nitride using a Berkovich indenter. The data consist of three sequential unloading-reloading cycles after reaching the initial peak load.

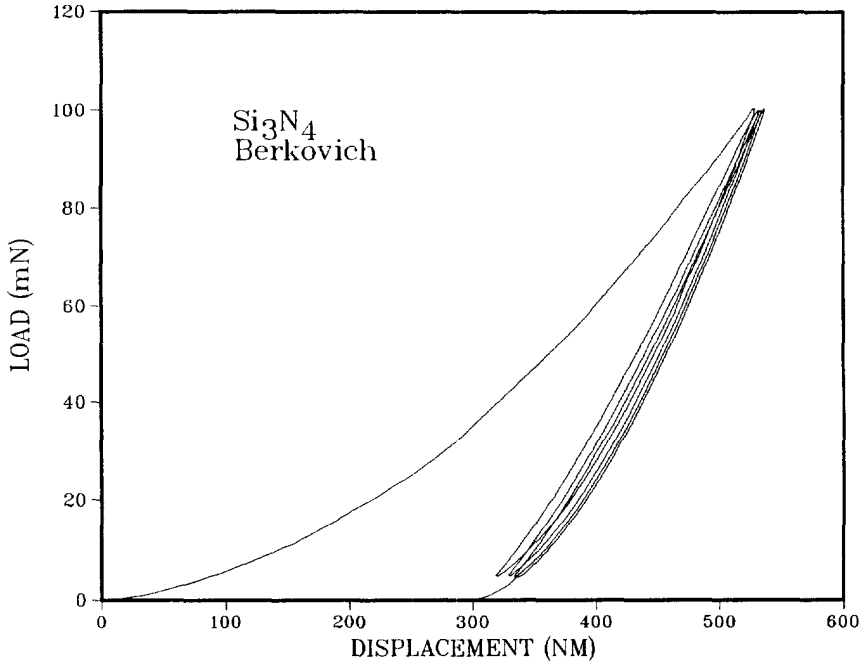

Fig. 12. Experimental load-displacement curves of 1070 steel using a cube corner indenter. The data consist of three sequential unloading-reloading cycles after reaching the initial peak load.

Tables 1 and 2 list the strength coefficient, k, strain hardening index n, and the experimental average hardness for 1070 steel and silicon nitride, respectively. Figure 14 compares the stress-strain curve of 1070 steel determined from the present study with experimental values from different sources. The agreement is good, considering the fact that only two points that lie well beyond the experimental data points were used to define the curve. One more set of experiments with a conical indenter whose included half-angle is more than 70.3° would yield a calculated point in the range of the compared experimental

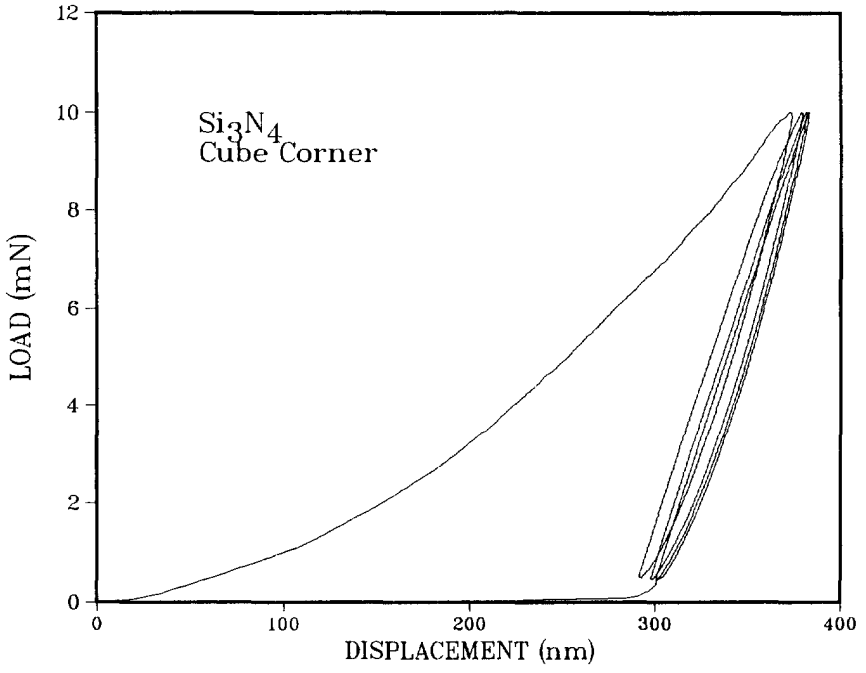

Fig. 13. Experimental load-displacement curves of silicon nitride using a cube corner indenter. The data consist of three sequential unloading-reloading cycles after reaching the initial peak load.

Table 1. Parameters determining the true stress-plastic strain curve of 1070 steel

Indenter	Characteristic Plastic Strain	Mean Hardness (GPa)	Flow Stress† (GPa)	Strength Coefficient‡ k (GPa)	Hardening Index‡ n
Berkovich	0.070	9.5	4.0	5.5	0.12
Cube Corner	0.225	10.8	4.6		

† Equation 5
‡ $\sigma = k\varepsilon_p^n$
Mean Reduced Elastic Modulus: 232 GPa

Table 2. Parameters determining the true stress-plastic strain curve of silicon nitride

Indenter	Characteristic Plastic Strain	Mean Hardness (GPa)	Flow Stress† (GPa)	Strength Coefficient‡ k (GPa)	Hardening Index‡ n
Berkovich	0.070	25.7	11.4	20.5	0.22
Cube Corner	0.225	32.6	14.8		

† Equation 5
‡ $\sigma = k\varepsilon_p^n$
Mean Reduced Elastic Modulus: 305 GPa

values. Figure 15 shows the stress-strain curve of silicon nitride with the two stress-strain coordinates determined from the ultra-hardness values.

The validity of eqn 5 was further checked by predicting the stress-plastic strain curves for copper (elastic modulus 115 GPa) and steel (elastic modulus 207 GPa). This was done based on the hardness measurements reported by Atkins and Tabor (1965) using different cone half-angles. The plastic strains for cone angles other than 70.3° and 42.3°, were obtained by fitting a straight line between these two values (Fig. 4). As seen in Fig 16 and 17, the calculated values are in very good agreement with known compressive stress-plastic strain curves for these two materials.

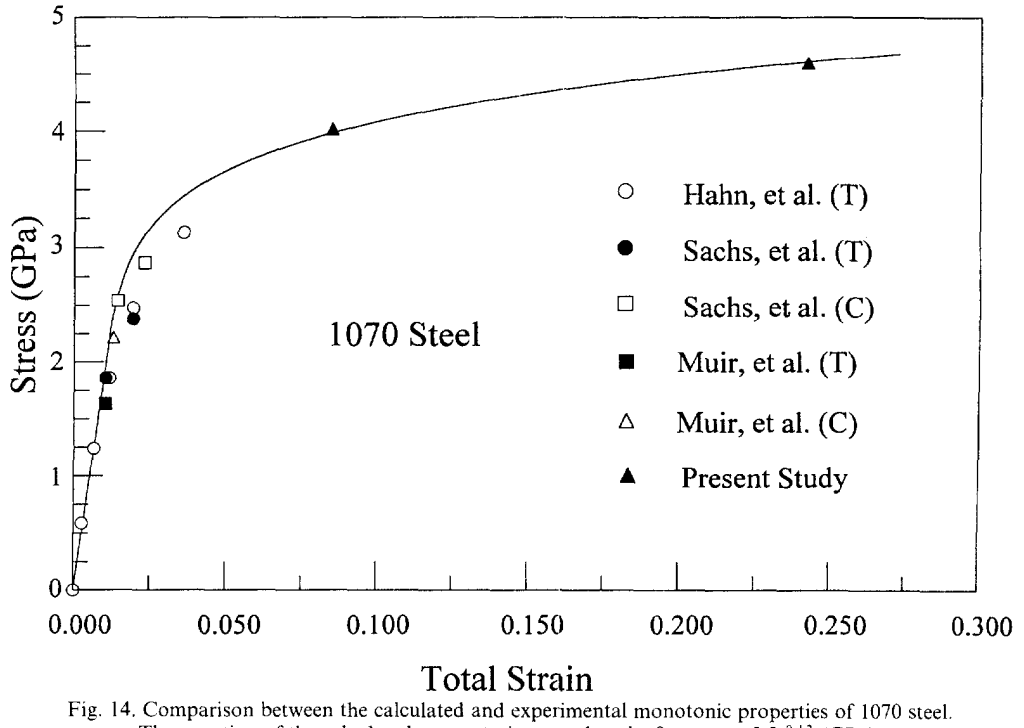

Fig. 14. Comparison between the calculated and experimental monotonic properties of 1070 steel. The equation of the calculated stress-strain curve has the form: $\sigma = 5.5\varepsilon_p^{0.12}$ (GPa).

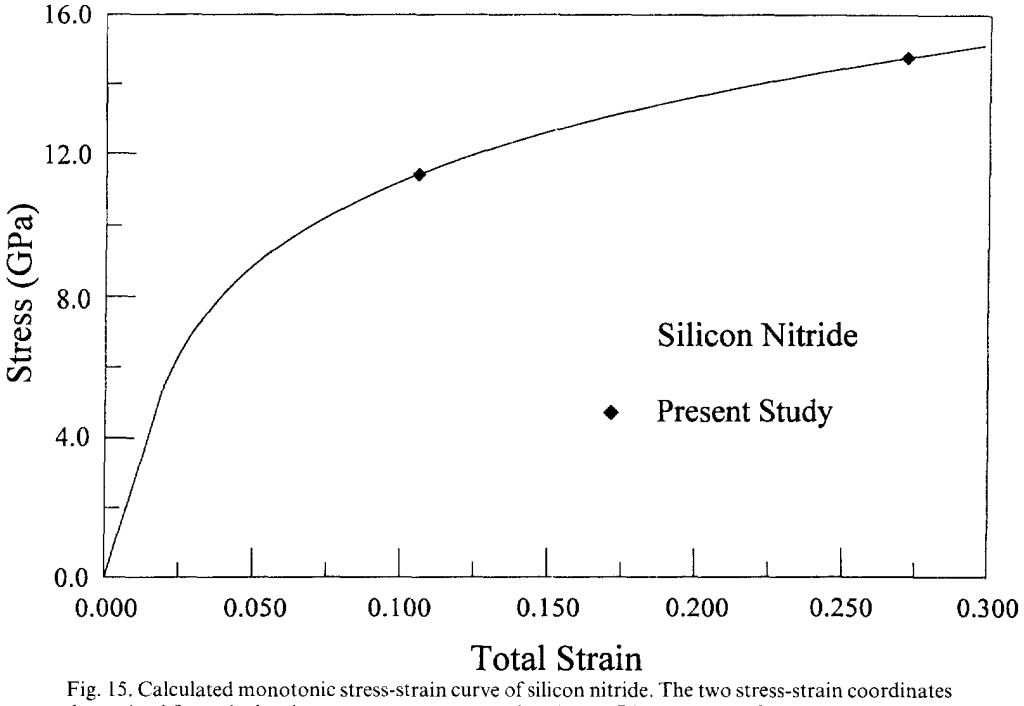

Fig. 15. Calculated monotonic stress-strain curve of silicon nitride. The two stress-strain coordinates determined from the hardness measurements are also shown. The equation of the calculated stress-strain curve has the form: $\sigma = 20.5\varepsilon_p^{0.22}$(GPa).

As mentioned by Pharr *et al.* (1993), the cracking threshold in most ceramics using a Vickers/Berkovich indenter is about 25 grams. This is well above the peak load of 10 grams applied to the Berkovich indenter in the present study. They suggest a cracking threshold of about 0.5 grams for most ceramics using a cube corner indenter. This is lower than the peak load of 1.0 gram applied using a cube corner indenter. Oliver and Pharr confirm in a personal communication that in this range, cracking may not affect the load-displacement

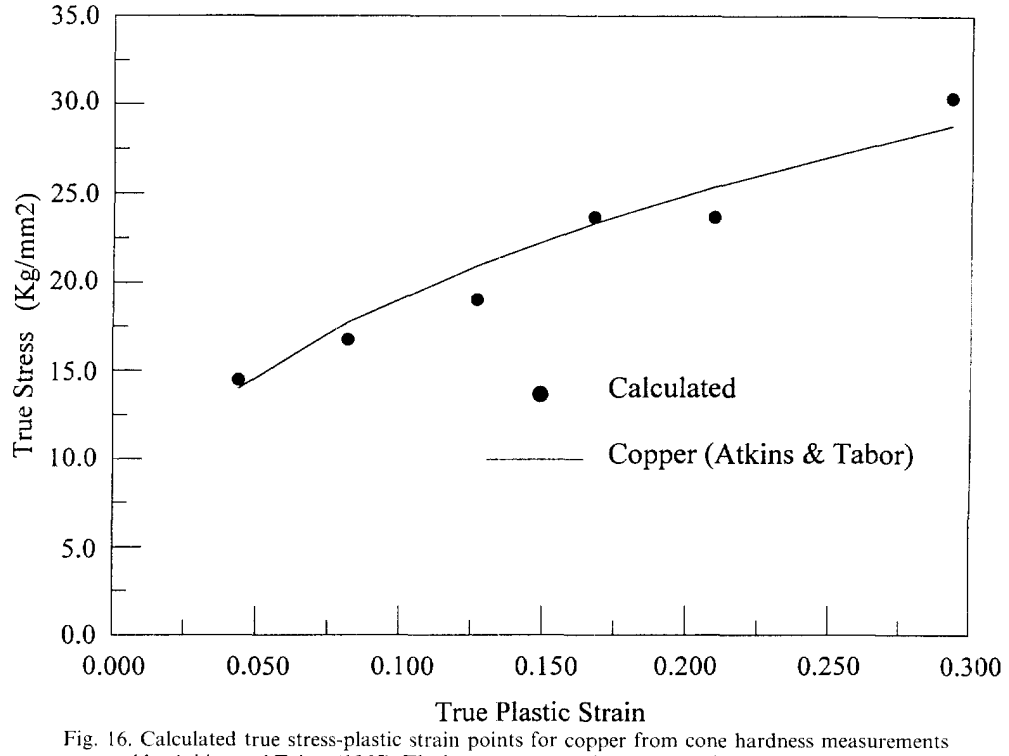

Fig. 16. Calculated true stress-plastic strain points for copper from cone hardness measurements reported by Atkins and Tabor (1965). The known compressive stress-strain curve for copper (elastic modulus: 115 GPa) is shown by the solid line (Atkins and Tabor, 1965).

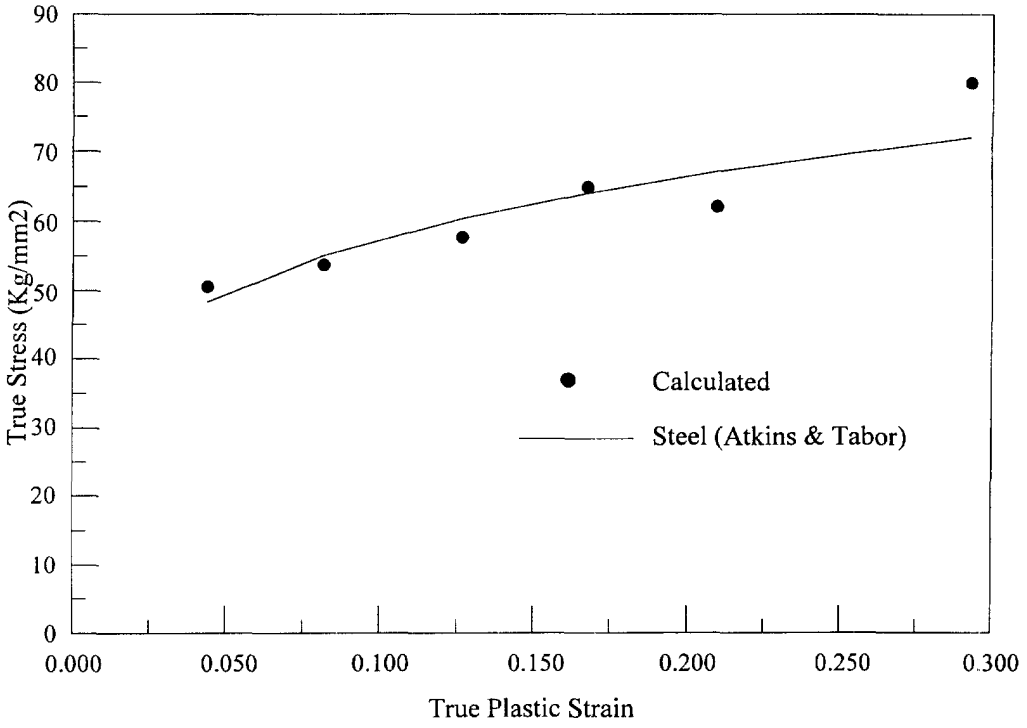

Fig. 17. Calculated true stress-plastic strain points for steel from cone hardness measurements reported by Atkins and Tabor (1965). The known compressive stress-strain curve for steel (elastic modulus: 207 GPa) is shown by the solid line (Atkins and Tabor, 1965).

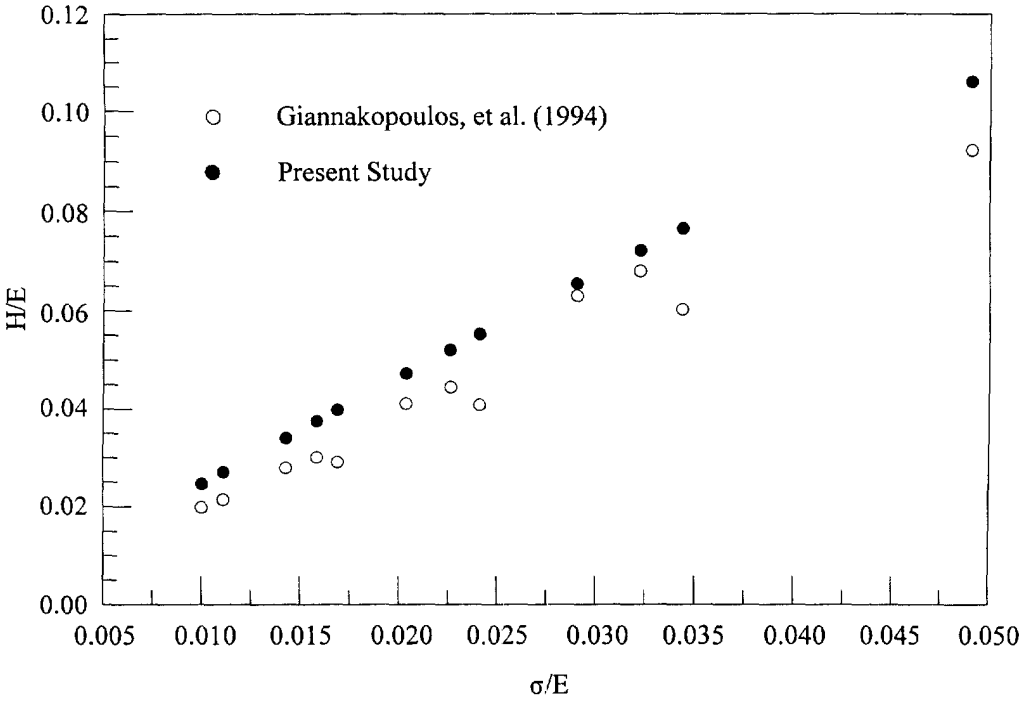

Fig. 18. Comparison of the calculated hardness to elastic modulus ratio variation with flow stress to elastic modulus ratio, for a 70.3° conical indenter, and a three-dimensional Vickers indenter (Giannakopoulos *et al*, 1994). The calculations were done with different material properties used in the analytical part of the present study.

curves. Since the evaluation of the monotonic and cyclic constitutive relations are based on the experimental load-depth data, it is reasonable to conclude that cracking of the specimen in this load range does not affect the results.

Very recently, Giannakopoulos *et al.* (1994) have performed three dimensional finite element analysis of Vickers indentation. For strain hardening materials, they find that the computed hardness H can be expressed as

$$H = 0.27(\sigma_o + \sigma_{0.3})\left(1 + \ln\frac{E\tan 22^\circ}{3\sigma_o}\right) \tag{9}$$

where σ_o is the initial yield strength, $\sigma_{0.3}$ is the flow stress at a plastic strain value of 0.3, and E is the elastic modulus of the material indented. Figure 18 compares the predicted hardness values, described by eqns 5 and 9, for the different material properties used in the analytical part of the present study. The flow stress at a plastic strain value of 0.07, normalized with respect to the elastic modulus, was used as the independent variable. As seen in Fig. 18, the H/E curve obtained using a three dimensional Vickers indenter lies below the curve obtained using a conical indenter of half-angle 70.3°. This discrepancy of about 16% is likely because small strain finite element analysis was used by Giannakopoulos *et al.* (1994) to obtain eqn 9. These workers report higher values of computed hardness (about 10% more for aluminum 7075-T6) when large strain theory was used in their analysis. Thus, it is reasonable to conclude that the hardness-flow stress correlation obtained from the present study, employing a simple axisymmetric model, is close to that obtained using a more complex, three dimensional analysis.

An important question to be addressed is the higher Berkovich hardness values (1070 steel-9.5 GPa; Silicon nitride-25.7 GPa) compared to the Vickers hardness values (1070 steel-7.5 GPa; Silicon nitride-16.0 GPa). Oliver (1994) believes that the difference in material pile-up between the two indenter geometries could be responsible for the difference. However, as discussed in the previous paragraph, since there is very little difference in the computed hardness values between a 70.3° conical and four sided pyramidal Vickers

indenter, it is unlikely that the three-sided pyramidal Berkovich hardness would be very different. Thus, it is difficult to explain the difference based on material pile-up alone. Also, any possible difference in the effective plastic strain beneath the two indenters may not be enough to increase the experimental Berkovich hardness values by about 30%. In fact, it may not be possible to attribute the hardness differences between the two indenters to any fundamental differences, such as, the indenter geometry. This is because the hardness values being compared involve different depths of penetration.

CONCLUSIONS

An elasto-plastic finite element model of the indentation produced by an instrumented, ultra-low-load hardness test using a Berkovich and cube corner indenter has been devised. A method has been suggested to obtain the characteristic plastic strain of geometrically similar indents. The results compare very well with the characteristic plastic strain values for macroscopic indents.

An equation relating the hardness to the flow stress of the material has been developed. This is independent of the deformation mode beneath the indenter. Comparing the results of the present study with those published by Giannakopoulos *et al.* (1994), suggests that a 70.3° conical indenter can very successfully model a three-dimensional Vickers indenter. The monotonic true stress–true strain curve obtained from the experimental hardness values, using the suggested characteristic plastic strain and hardness–flow stress correlation, compares well with the known monotonic stress–strain relationship for 1070 steel. The monotonic stress-strain curve of silicon nitride has been determined from the experimental load–depth data.

Acknowledgements—The authors with to thank Hibbit, Karlsson, and Sorensen, Inc. for permission to use the finite element code ABAQUS, and the National Center for Supercomputing Applications (NCSA) at the University of Illinois at Urbana-Champaign. The authors also wish to express their appreciation to the National Science Foundation (Grant # 9203252) and the Jacob Wallenburg Foundation of Sweden for providing funding for this project.

REFERENCES

Atkins, A. G. and Tabor, D. (1965). Plastic indentation in metals with cones. *Journal of the Mechanics and Physics of Solids* **13,** 149–164.

Bhattacharya, A. K. and Nix, W. D. (1988). Finite element simulation of indentation experiments. *International Journal of Solids and Structures* **24,** 881–891.

Bhattacharya, A. K. and Nix, W. D. (1991). Finite element analysis of cone indentation. *International Journal of Solids and Structures* **27,** 1047–1058.

Bishop, R. F., Hill, R. and Mott, N. F. (1945). The theory of indentation and hardness tests. *The Proceedings of the Physical Society* **57,** 147.

Bourcier, R. J., Stone, C. M. and Yost, F. G. (1985). A numerical and experimental study of the indentation hardness test. Sandia report no. SAND85-0486; Sandia National Laboratory, Albuquerque.

Cai, X and Zhou, P. N. (1992). Influence of elastic recovery on microindentation hardness—a finite element analysis. *Scripta Metallica et Materiala* **27,** 347–352.

Doerner, M. F. and Nix, W. D. (1986). A method of interpreting the data from depth-sensing indentations measurements. *Journal of Materials Research* **4,** 601.

Giannakopoulos, A. E., Larrson, P. L and Vestergaard, R. (1994). Analysis of Vickers indentation. *International Journal of Solids and Structures* **31,** 2679–2708.

Hill, R. (1950). *The Mathematical Theory of Plasticity*. University Press, Oxford.

Hirst, W. and Howse, M. G. J. W. (1969). Title. *Proceedings, Royal Society* **A311,** 429.

Johnson, K. L. (1970). The correlation of indentation experiments. *Journal of the Mechanics and Physics of Solids* **18,** 115–126.

Lee, C. H., Masaki, S. and Kobayashi, S. (1972). Analysis of ball indentation. *International Journal of Mechanical Sciences* **14,** 417.

Marsh, D. M. (1964). Plastic flow in glass. *Proceedings, Royal Society* **A279,** 420–435.

Mulhearn, T. O. (1959). Title. *Journal of the Mechanics and Physics of Solids* **7,** 85.

Oliver, W. C. (1992). *Nanoindenter® reference manual.*

Oliver, W. C. and Pharr, G. M. (1992). An improved technique for determining hardness and elastic modulus using load and displacement sensing indentation experiments. *Journal of Materials Research* **7,** 1564–1583.

Pethica, J. B., Hutchings, R. and Oliver, W. C. (1983). Hardness measurements at penetration depths as small as 20 nm. *Philosophical Magazine A* **48,** 593–606.

Pharr, G. M., Harding, D. S. and Oliver, W. C. (1994). Cracking during nanoindentation and the measurement of fracture toughness at small scales. Report No. 94-17, Institute for Mechanics and Materials, LOCATION, pp. 81–82.

Prandtl, L. (1920). *Nachr. Ges. Wiss.*, Gottingen, Math. Phys. K1., 74.
Rubinstein, C. (1981). A critical appraisal of static hardness measurements. *Journal of Applied Mechanics* **48,** 796–802.
Samuels, L. E. and Mulhearn, T. O. (1957). Article title. *Journal of the Mechanics and Physics of Solids* **5,** 125.
Sneddon, I. N. (1965). The relation between load and penetration in the axisymmetric Boussinesq problem for a punch of arbitrary profile. *International Journal of Engineering Science* **3,** 47–57.
Tabor, D. (1951). *The Hardness of Metals*. Clarendon Press, Oxford.
Tanega, A. G. and Hurkx, G. A. M. (1986). The determination of stress-strain curves of thin layers using indentation tests. *Journal of Engineering Material Technology* **108,** 230–232.